# Adaptive Total Variation Regularization Based SAR Image Despeckling and Despeckling Evaluation Index

Yao Zhao, Jian Guo Liu, *Member, IEEE*, Bingchen Zhang, Wen Hong, *Member, IEEE*, and Yi-Rong Wu, *Member, IEEE*

***Abstract*—We introduce a total variation (TV) regularization model for synthetic aperture radar (SAR) image despeckling. A dual-formulation-based adaptive TV (ATV) regularization method is applied to solve the TV regularization. The parameter adaptation of the TV regularization is performed based on the noise level estimated via wavelets. The TV-regularization-based image restoration model has a good performance in preserving image sharpness and edges while removing noises, and it is therefore effective for edge preserve SAR image despeckling. Experiments have been carried out using optical images contaminated with artificial speckles first and then SAR images. A despeckling evaluation index (DEI) is designed to assess the effectiveness of edge preserve despeckling on SAR images, which is based on the ratio of the standard deviations of two neighborhood areas of different sizes of a pixel. Experimental results show that the proposed ATV method can effectively suppress SAR image speckles without compromising the edge sharpness of image features according to both subjective visual assessment of image quality and objective evaluation using DEI.**

***Index Terms*—Adaptive total variation (ATV) regularization, despeckling, evaluation index, synthetic aperture radar (SAR).**

## I. Introduction

SYNTHETIC aperture radar (SAR) is an important technology for various remote sensing applications such as Earth environment monitoring, geohazard investigation, etc., with the capability of all-weather and all-time observation. However, due to its imaging mechanism, SAR images suffer from speckles that subdue the visual quality of images for interpretation and hinder the automatic information extraction using image processing tools [1]. Hence, despeckling is an important issue in SAR image processing.

Many algorithms have been developed for speckle suppression. In general, there are two major classes of despeckling methods. One class is multilook processing, which is mainly an incoherent addition of independent images (looks) of the same scene. The major drawback of this method is degradation of image resolution. The other class is filtering. The Lee [2], Frost [3], Kuan [4], and adaptive median filters are typical examples of such techniques. These conditional low-pass filtering based techniques are simple and have high processing efficiency but show limitations on either preserving image sharpness or effective speckle suppression, and the performance is scene dependent. With increased complexity, wavelet-based algorithms [5]–[7] as well as the methods based on the so-called second generation wavelets [8], curvelets [9], shearlet [10], bandelets [11], etc., formulate another brunch of despeckling techniques. These techniques can deliver better performance on edge preserve despeckling, but artifacts often occur. Despeckling can be considered as a statistical estimation problem which can be resolved with linear filtering constrained under maximum *a posteriori* (MAP) or maximum likelihood criterion [12]. However, it is difficult to provide an accurate probability distribution of scene for the MAP filtering; moreover, its processing efficiency is low. By exploiting image self-similarity following the structure of block-matching 3-D algorithm, nonlocal filtering [13] takes the wavelet subband mean vector of a group of pixels surrounding a target pixel to suppress the speckles. The algorithm can achieve impressive despeckling results; however, it exhibits a remarkable complexity with high computing cost, and its performance is dependent on a user input parameter.

The total variation (TV) regularization based image restoration model was introduced by Rudin, Osher, and Fatemi [14], and it has raised wide research interests in digital image processing and computer vision. It has a good performance in preserving image sharpness and edges while removing noises. TV regularization is based on the minimization of the energy, which is the combination of two types of information: a data fitting term and a regularization term. The data fitting term ensures the processed image to be an approximation of the original, and the regularization term imposes restrictions for smoothness. The TV regularization has been adopted as a reconstruction method in compressed sensing [15] for sparse signal processing. The link between the TV regularization and sparse representation is given in [16].

This paper presents a SAR image despeckling method based on adaptive TV (ATV) regularization. First, the speckle noise level of the SAR image is estimated based on the wavelet

Manuscript received September 13, 2013; revised August 11, 2014; accepted October 13, 2014. Date of publication November 12, 2014; date of current version January 7, 2015. This work was supported in part by the National Basic Research Program of China under Grant 2010CB731900 and by the CAS/SAFEA International Partnership Program for Creative Research Teams.

Y. Zhao is with the Science and Technology on Microwave Imaging Laboratory, Institute of Electronics, Chinese Academy of Sciences, Beijing 100190, China, and also with No. 23 Institute of the Second Academy, CASIC, Beijing 100854, China (e-mail: yaozhao@mail.ie.ac.cn).

J. G. Liu is with the Department of Earth Science and Engineering, Imperial College London, SW7 2AZ London, U.K. (e-mail: j.g.liu@imperial.ac.uk).

B. Zhang, W. Hong, and Y.-R. Wu are with the Science and Technology on Microwave Imaging Laboratory, Institute of Electronics, Chinese Academy of Sciences, Beijing 100190, China.

Digital Object Identifier 10.1109/TGRS.2014.2364525

analysis. Then, a parameter adaptation of TV regularization is exploited according to the estimated noise level. Finally, a semi-implicit gradient descent method is proposed to solve the dual formulation of TV regularization. For objective assessment of the performance of SAR image despeckling, a despeckling evaluation index (DEI) is designed and tested. The experimental results show that the proposed ATV method can effectively suppress the speckles of SAR image with good preservation of the sharpness of edges as confirmed by both the DEI and visual assessment.

This paper is organized as follows. In Section II, we describe the model and the algorithm of the TV-regularization-based SAR image despeckling method. Section III introduces the evaluation index for despeckling performance. Section IV presents the experimental results and assessment. The conclusion is presented in Section V.

## II. Model and Algorithm: TV-Regularization-Based SAR Image Despeckling

### A. TV Model

We presume that the despeckled SAR image $f$ can be obtained from a SAR image $g$ by minimization of the objective function given as

$$\min_f \left\{ \frac{1}{2}\|f-g\|^2 + \lambda \mathrm{TV}(f) \right\} \tag{1}$$

where $\lambda > 0$ is a regularization parameter and $\mathrm{TV}(f) = \|\nabla f\|_1$ is the TV norm of $f$. The objective function is the weighted sum of a fit to the data and a regularization term. The regularization parameter $\lambda$ controls the balance between the two terms. If $\lambda$ is too large, the despeckled image will be oversmoothed, and otherwise, if $\lambda$ is too small, the speckles will not be sufficiently eliminated.

To solve the model (1), we first estimate the noise variance $\sigma$ of the image. Supposing that $\sigma$ is additive white Gaussian noise (AWGN), it can then be estimated by the formula [17]

$$\sigma = \mathrm{median}(|d_k|)/.6745 \tag{2}$$

where $d_k$ is the elements of the detail wavelet coefficient vector of the speckled image.

Here, we need to indicate that the speckle noise in SAR image is usually modeled as $g = f + r \times f$, where $r$ is the random noise with mean of zero and variance of $\sigma^\star$ [1]. This is a multiplicative noise. However, for image display, a logarithm transform is usually applied to the original speckled image. In this case, $\log(g) = \log(r+1) + \log(f)$. The logarithm operation transforms the multiplicative noise of the SAR speckling model into an additive one and thus fits to formula (2) under the hypothesis of the AWGN noise model.

Many algorithms have been proposed for the TV regularization (1), such as time-marching scheme [14], Newton's method [18], fixed-point iteration method [19], Bregman iterative [20], and Chambolle's method [21]. Here, we choose the Chambolle's method to solve the TV regularization. The idea of the Chambolle's method is to achieve the optimization of image $f$ by the optimization of vector field $\omega^\star$. The despeckled image $f$ is related to $\omega^\star$ by $f = g - \lambda \mathrm{div}(\omega^\star)$. The optimization of vector field can then be solved by projected gradient descent method as

$$\omega^{k+1} = \mathrm{proj}\left(\omega^k - \tau \nabla\left(\mathrm{div}(\omega^k - g/\lambda^k)\right)\right) \tag{3}$$

where proj denotes the orthogonal projector on the constraint $\|\omega\|$. It can be proved that, when the step size $\tau$ satisfies $0 < \tau < 1/4$, $g - \lambda \mathrm{div}(\omega^k)$ converges to $f$ for $k \to \infty$ [21].

In [22], an adaptation algorithm for parameter $\lambda$ is proposed based on the noise level and the current estimation of the despeckled image by transforming (1) to the following constraint minimization:

$$\min_f \mathrm{TV}(f), \qquad \text{s.t.} \quad \|f-g\| \le \varepsilon$$

where $\varepsilon = \sqrt{N}\sigma$ is the noise level and $N$ is the total number of pixels of the SAR image. Recall that the solution at the step $k$ is $f^k = g - \lambda \mathrm{div}(\omega^k)$; then, $\lambda^k$ at step $k$ is updated as

$$\lambda^{k+1} = \lambda^k \sqrt{N}\sigma / \|f^k - g\|. \tag{4}$$

TABLE I
Estimation of Noise Variance $\sigma$ Using Five Wavelets for Different Scenes of an ERS SAR Image

| | Sea | Mountain | Plain | All |
|---|---|---|---|---|
| **bior 4.4** | 10.6061 | 12.2536 | 11.2492 | 12.2289 |
| **bior 6.8** | 9.7373 | 11.4689 | 10.3821 | 11.6611 |
| **db 5** | 10.9641 | 12.8518 | 11.7217 | 12.8302 |
| **db 6** | 11.0380 | 12.7299 | 11.8122 | 12.7920 |
| **db 7** | 10.8415 | 12.6126 | 11.6597 | 12.7251 |

TABLE II
DEI of Different Window Sizes for an ALOS SAR Image (Without Despeckling)

| m \ n | 11 | 13 | 15 | 17 | 19 | 21 | 23 | 25 |
|---|---|---|---|---|---|---|---|---|
| **3** | 0.3241 | 0.2969 | 0.2756 | 0.2584 | 0.2441 | 0.2320 | 0.2215 | 0.2124 |
| **5** | 0.5403 | 0.5063 | 0.4793 | 0.4571 | 0.4383 | 0.4222 | 0.4081 | 0.3955 |
| **7** | 0.6523 | 0.6149 | 0.5848 | 0.5599 | 0.5386 | 0.5203 | 0.5042 | 0.4900 |
| **9** | 0.7269 | 0.6872 | 0.6552 | 0.6285 | 0.6057 | 0.5859 | 0.5685 | 0.5530 |

### B. Choice of $\sigma$

Obviously, the choice of $\sigma$, the noise variance, is a key issue for the initiation and update of parameter $\lambda$. Supposing that a nonspeckle SAR image is piecewise smooth, then after a wavelet transform, most of the detail (high-frequency information) coefficients of the wavelet should be close to zero. This implies that the small nonzero detail coefficients of the wavelet of an original SAR image approximate the detail coefficients of the wavelet of speckle noise. In other words, "most" of the empirical wavelet detail coefficients are corresponding to noise. Thus, $\sigma$ is estimated using (2), but this is only a rough estimation because of the following.

1) The estimation of $\sigma$ varies considerably with the wavelet algorithm and parameters used.
2) The estimation of $\sigma$ is not scene independent. The estimated $\sigma$ value from a smooth scene will be lower than a scene with complicated edge textures.

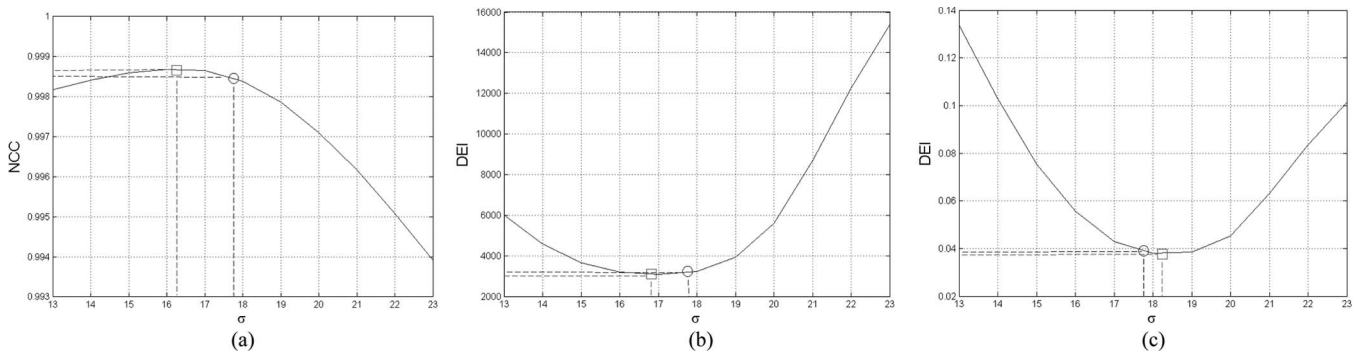


Fig. 1. (a) Plot of $\sigma$ against NCC between the original and despeckled Lena images. (b) Plot of $\sigma$ against DEI (window size: numerator $3 \times 3$; denominator $19 \times 19$). (c) Plot of $\sigma$ against DEI (window size: numerator $5 \times 5$; denominator $19 \times 19$). The circles denote the values corresponding to (2) predicted $\sigma$, and the squares denote the maximum/minimum values of NCC and DEI.

Estimation of $\sigma$ varies with the choice of wavelet algorithms and the scene complexity. Table I presents the estimation of $\sigma$ using different types of wavelets for different scenes in a European Remote Sensing Satellite (ERS) image including sea, mountain, and plain. In Table I, bior 4.4 and bior 6.8 represent the biorthogonal wavelets with 4/4 and 6/8 vanishing moments, and db5, db6, and db7 represent Daubechies wavelets with 5, 6, and 7 vanishing moments. We have chosen bior 4.4 wavelets empirically for the experiments presented in this paper. The variation of $\sigma$ is about 20% between different scenes and between different algorithms. This means that it is not realistic and practical to achieve a precise and unique estimation of $\sigma$; instead, we shall demonstrate in experiments that, because of the adaptive optimization mechanism of the ATV algorithm, a rough estimation of $\sigma$ is adequate to initiate the ATV despeckling in the range of a global optimization, and then, the adaptive iteration will reach the local optimization of despeckling.

## III. DEI

The performance assessment for SAR image despeckling is not straightforward because the original nonspeckle SAR image is unknown. We therefore first used simulated speckled images to evaluate the performance of our method in comparison with that of other commonly used and new techniques. In this case, both the original speckle free images and added speckles are known, and the despeckling results can be visually compared with the original images as well as benchmarked using evaluation indices. Then, the same performance assessment procedure can be applied to the SAR images of various landscapes.

For simulated speckled images, the normalized cross-correlation coefficient (NCC) can be used to assess the similarity between the despeckled image and the original.

To assess the performance of edge preserve despeckling for SAR images, a DEI is designed based on a ratio between the standard deviation (std) over a small neighborhood and that over a larger neighborhood, as defined in the following:

$$\mathrm{DEI} = \frac{1}{N}\sum_{i,j}\frac{\min\limits_{|p-i|<s,|q-j|<s}\left(\mathrm{std}(W^m_{p,q})\right)}{\mathrm{std}(W^n_{i,j})}, \qquad m<n \quad (5)$$

where $N$ is the total number of pixels in the SAR image; $W^n_{i,j}$ denotes the moving window centered at pixel $(i,j)$ with size of $n \times n$ in the denominator; the same notation applies for the numerator and $m < n$. The numerator is the minimum standard deviation of the $m \times m$ window roaming in a neighborhood no greater than $s \times s$, and $s < n$, around and include the pixel $(i,j)$. The summation is performed over the whole image.

TABLE III
NCC AND DEI OF EIGHT DESPECKLING METHODS FOR THREE STANDARD TEST IMAGES

| Algorithms | Pepper (NCC/DEI) | Lena (NCC/DEI) | Boat (NCC/DEI) |
|---|---|---|---|
| Lee | 0.9949/0.3290 | 0.9957/0.3476 | 0.9944/0.3512 |
| Frost | 0.9971/0.1431 | 0.9980/0.1392 | 0.9971/0.1508 |
| Mean | 0.9968/0.1655 | 0.9969/0.1655 | 0.9958/0.1655 |
| Median | 0.9980/0.1106 | 0.9977/0.1191 | 0.9968/0.1300 |
| A-median | 0.9913/0.4295 | 0.9913/0.4271 | 0.9921/0.3881 |
| Shearlet | 0.9975/0.2680 | 0.9974/0.2769 | 0.9977/0.2744 |
| Nonlocal | 0.9982/**0.0371** | **0.9986**/0.0407 | 0.9981/0.0422 |
| ATV | **0.9984**/0.0389 | 0.9985/**0.0385** | **0.9982/0.0390** |

For a despeckled SAR image of a smooth area without topographic edges

$$\mathrm{std}(W^n_{i,j}) \approx \min_{|p-i|<s,|q-j|<s}\left(\mathrm{std}(W^m_{p,q})\right)$$

and the DEI as a ratio defined in (5) approximates to 1. In areas which are rich of edges, the denominator of (5) calculated using a larger window would be much greater than the numerator calculated as the minimum of a smaller window roaming in a neighborhood if the despeckling is effective, and thus, the ratio should be much less than 1. Thus, the smaller the DEI is, the better the edge preserve despeckling ability. As a ratio of standard deviation, DEI is robust to the contrast variation of images.

The choice of window size can affect the performance of the DEI. The denominator window must be large enough to cover at least one true edge feature, and therefore, the window size relates to image textual feature characteristics and image spatial resolution. Table II presents the DEI values calculated from the original single-look Advanced Land Observation Satellite (ALOS) SAR image used in our experiments (see Fig. 3) for different window sizes of numerator and denominator. The data show that DEI varies with the size of calculation windows; it increases with the increase of numerator window size and decreases with the increase of the denominator window size. This is because, in this edge-rich mountainous area covered by the image, increasing window size will include more edges and

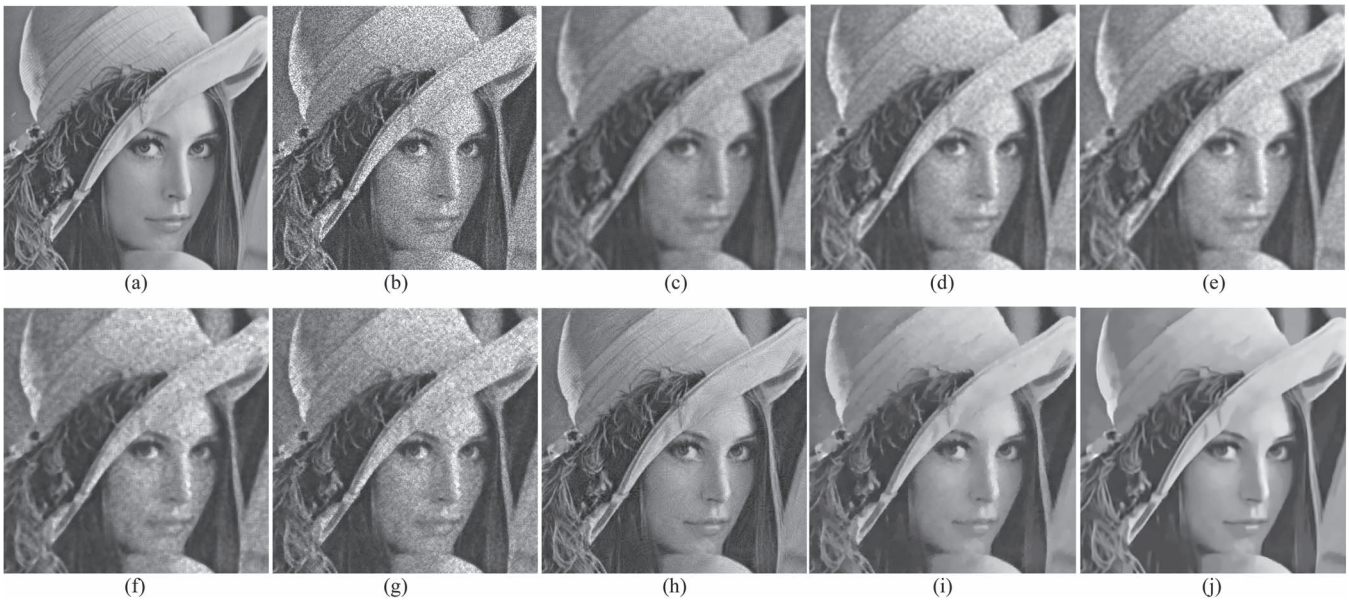


Fig. 2. Despeckling experimental results of the Lena image. The filters used in (c)–(g) are $5 \times 5$. (a) Original image. (b) Speckled. (c) Lee. (d) Frost. (e) Mean. (f) Median. (g) Adaptive median. (h) Shearlet. (i) ATV. (j) Nonlocal.

thus generally increase the standard deviation for either numerator or denominator. The increase of the numerator increases DEI, while the increase of the denominator decreases DEI.

The DEI is used for relative assessment among different despeckling techniques applied to the same image, and the lowest DEI indicates the most effective edge preserve despeckling technique. In this sense, the DEI is robust to its scene dependence of window size for effective assessment and ranking of despeckling performance, as further discussed based on experiments in the end of the following section. In all circumstances, 0.1 drop in DEI value indicates a significant improvement in despeckling.

## IV. Experimental Results and Analysis

### A. Simulated Speckled Images

The experiments were carried out using several well-known test optical images, including Pepper, Lena, and Boat. These images were contaminated by adding white Gaussian noise with a variance of 18. The variances estimated by (2) for three images are 18.2145, 17.8563, and 18.2454, respectively, indicating that the noise variance estimation by (2) is considerably accurate.

We first investigated the influence of the noise variance $\sigma$ in our algorithm to confirm that the updating of $\lambda$ in (4) is reasonable. For the Lena image, plots of $\sigma$ against NCC between the original and despeckled images, and $\sigma$ against DEI (numerator window size $= 3$ and 5 and denominator window size $= 19$) are presented in Fig. 1. It is interesting to notice that the $\sigma$ value of the maximum NCC is about 1.5 shifting to the left from the predicted $\sigma$ value by (2) and those of the minimum DEIs of $3 \times 3$ and $5 \times 5$ numerator windows are about 1 shifting to the left and only 0.3 shifting to the right, respectively. The discrepancies are less than the variation of $\sigma$ values that resulted from the choice of wavelet algorithms and scene dependence presented in Table I. As the predicted $\sigma$ values by (2) and the $\sigma$ values corresponding to the maximum NCC and minimum DEI are all in the relatively flat peak and trough parts of the curves in Fig. 1, their variation within a range is insensitive to the values of NCC and DEI. For instance, the NCC value at the predicted $\sigma$ is $\sim$0.0003 below the maximum NCC, while the DEI values at the predicted $\sigma$ are less than 0.0004 above the minimum DEIs for both two numerator window sizes.

Depending on the numerator window size, the $\sigma$ value of the minimum DEI can be either slightly greater or smaller than the $\sigma$ predicted by (2). This indicates that the estimation of $\sigma$ by (2) is nearly optimal and surely robust. For both numerator window sizes, the $\sigma$ values corresponding to the minimal DEIs are greater than that corresponding to the maximum NCC, which is $\sim$1.7 less than the true $\sigma$ value of 18. This implies that NCC based on areal comparison is overly favorable to smoothness (despeckling), while DEI keeps a balance between smoothness and edge preservation. In particular, the $\sigma$ corresponding to the DEI minima calculated using $5 \times 5$ numerator window is very near the true noise $\sigma$ (18); this numerator window size was thus chosen in further despeckling experiments using simulated speckled images and SAR images.

We then compared our algorithm with seven other despeckling methods: Lee filter [2], Frost filter [3], average filter, median filter, adaptive median (A-mean) filter, shearlet transform [10], and nonlocal filtering [13]. The shearlet transform and nonlocal filtering algorithms are new and complicated. We downloaded the author-provided codes to carry out the despeckling experiments using the default parameters which produced the best results. Table III presents the NCC values between the original and despeckled images using these algorithms and the corresponding DEIs calculated using $5 \times 5$ numerator window and $19 \times 19$ denominator window; in the table, the numbers in bold font are the highest NCC and lowest DEI. For the Pepper and Boat images, ATV achieved the highest NCC, while for the Lena image, ATV is 0.0001 lower than nonlocal filtering.

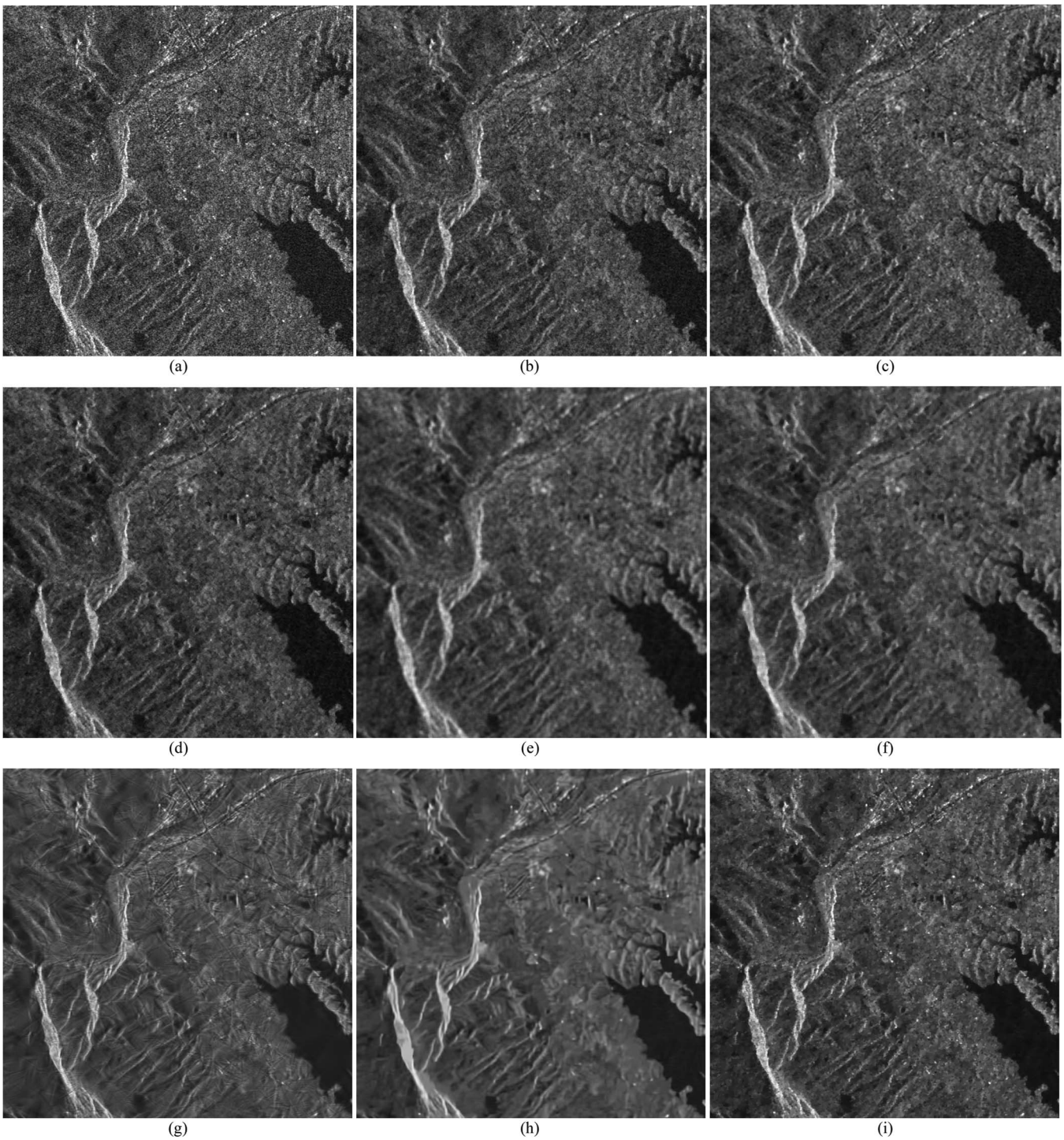


Fig. 3. Despeckling experimental results of an ALOS L-band SAR image. The filters used in (b)–(f) are $5 \times 5$. (a) Original image. (b) Lee filter. (c) Frost filter. (d) Adaptive median filter. (e) Mean filter. (f) Median filter. (g) Shearlet transform. (h) Nonlocal filtering. (i) ATV regularization.

The variation in performance between different test images may due to the image features. ATV achieved the lowest DEIs for the Lena and Boat images, while the lowest DEI of the Pepper image was delivered by nonlocal filtering. The ranking orders of DEIs for the three test images are largely consistent to that of NCC. The only exception is shearlet transform that is always ranked much lower by DEI than by NCC. We shall explain.

For illustration, Fig. 2 presents the results of the Lena image. It is visually self-evident that the performance of ATV is superior to the conventional despeckling filters [Fig. 2(c)–(g)]. The result of shearlet transform [Fig. 2(h)] with high NCC appears to be good viewed in small image with reduced resolution but in full resolution, severe artifacts of crackle texture occur, which will be further illustrated later in the discussion of SAR image despeckling results [see Fig. 4(a)]. The artifacts cannot be eliminated by fine-tuning the software parameters. This is why shearlet transform is consistently depicted by DEI as a poor performer (the third worst among the eight algorithms)

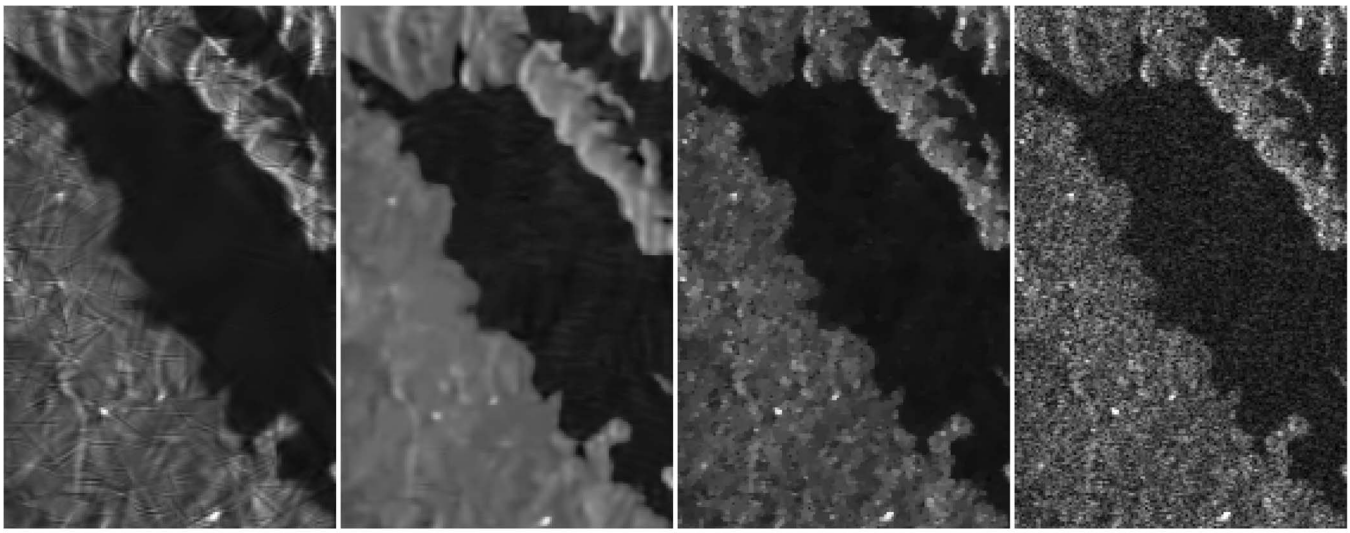


Fig. 4. Artifacts introduced by shearlet transform and nonlocal filtering despeckling algorithms. (a) Shearlet transform. (b) Nonlocal filtering. (c) ATV regularization. (d) Original.

with relatively high values, showing that DEI is very effective in spotting the defects of artificial textures. The image of nonlocal filtering [Fig. 2(i)] looks slightly better than the ATV image in terms of both patchwise smoothness and edge preservation, although its DEI value is slightly higher than that of ATV. In the SAR image experiment, we found that the nonlocal filtering may introduce subtle textural artifacts [see Fig. 4(b)]. Moreover, ATV is nearly 45 times faster than nonlocal filtering; it took 2.8873 s for ATV to complete Lena image despeckling, while for nonlocal filtering, it is 128.8119 s using the same desktop PC.

TABLE IV
DEI OF EIGHT DESPECKLING METHODS FOR MOUNTAIN AREA SAR IMAGES

| Rank | Algorithms | ALOS DEI | ERS DEI | Algorithms |
|---|---|---|---|---|
| 9 | Original | 0.4383 | 0.3723 | Original |
| 8 | A-median | 0.2557 | 0.3133 | Lee |
| 7 | Lee | 0.2477 | 0.2256 | A-median |
| 6 | Frost | 0.2362 | 0.1937 | Shearlet |
| 5 | Shearlet | 0.1739 | 0.1893 | Frost |
| 4 | Mean | 0.1632 | 0.1785 | Nonlocal |
| 3 | Median | 0.1435 | 0.1655 | Mean |
| 2 | Nonlocal | 0.1107 | 0.1426 | Median |
| 1 | ATV | 0.0753 | 0.1145 | ATV |

### *B. Results From SAR Images*

Several scenes of L-band SAR images of Japanese ALOS and C-band SAR images of ERS were processed to test the despeckling performance of the ATV regularization in comparison with the other seven despeckling techniques.

Fig. 3 presents the despeckling results for a single-look ALOS L-band SAR amplitude (intensity) image of a mountain-to-hill transition area with some urban features and roads. Such an area is effective in testing the despeckling performance in high relief as well as in flat landscape. For effective illustration, only part of this $1024 \times 1024$ scene is presented in Fig. 3 to show the despeckling results of $5 \times 5$ Lee, Frost, median, mean, and adaptive median filters; shearlet transform; nonlocal filtering; and ATV regulation. Observing Fig. 3, it is visually obvious that both nonlocal filtering and ATV regularization images [Fig. 3(g) and (h)] are better edge preserve despeckled than other techniques. The effectiveness of edge preservation is particularly demonstrated by the road junction and its nearby urban area in the upper-middle part of the images. With much longer processing time, the nonlocal filtering is more effective in despeckling than ATV, although its result is a bit overly smoothed, making the edges less sharp. The shearlet transform image appears to be smooth and edge sharp, but it is severely subdued by "ghost" texture artifacts (the same as in the Lena image experiment) as clearly illustrated in the zoomed-in image in Fig. 4(a). In the flat area, the reservoir in the bottom-right corner of the image presents a good benchmark of despeckling. The reservoir in the ATV image is clean without speckles. The $5 \times 5$ mean filter achieved similar despeckling performance but at the cost of significant edge blur. In the rest of despeckled images using conventional filtering algorithms, residual speckles are obvious in this still water body. The result of nonlocal filtering shows very effective despeckling; however, in the reservoir, some artificial ripples can be observed on the water surface by close look as illustrated in Fig. 4(b). This artifact largely in horizontal direction can also be faintly observed in areas other than the still water body. Careful screening also revealed that the algorithm may generate homogenous artificial blobs of several tens of pixels in size. In comparison, the ATV image [Fig. 4(c)] appears blockier than the nonlocal filtering image, but it has higher fidelity to the original image [Fig. 4(d)]; there is slight intensity variation in the reservoir corresponding to the trend encoded in the original image. The DEI values of all of the despeckled images are calculated using $5 \times 5$ numerator window and $19 \times 19$ denominator window as shown in Table IV, listed in a descending order of DEI. The DEI value of nonlocal filtering image is the second lowest but considerably (32%) greater than that of the ATV image. The possible reasons are oversmoothed patchwisely and stealth artifacts. The visual

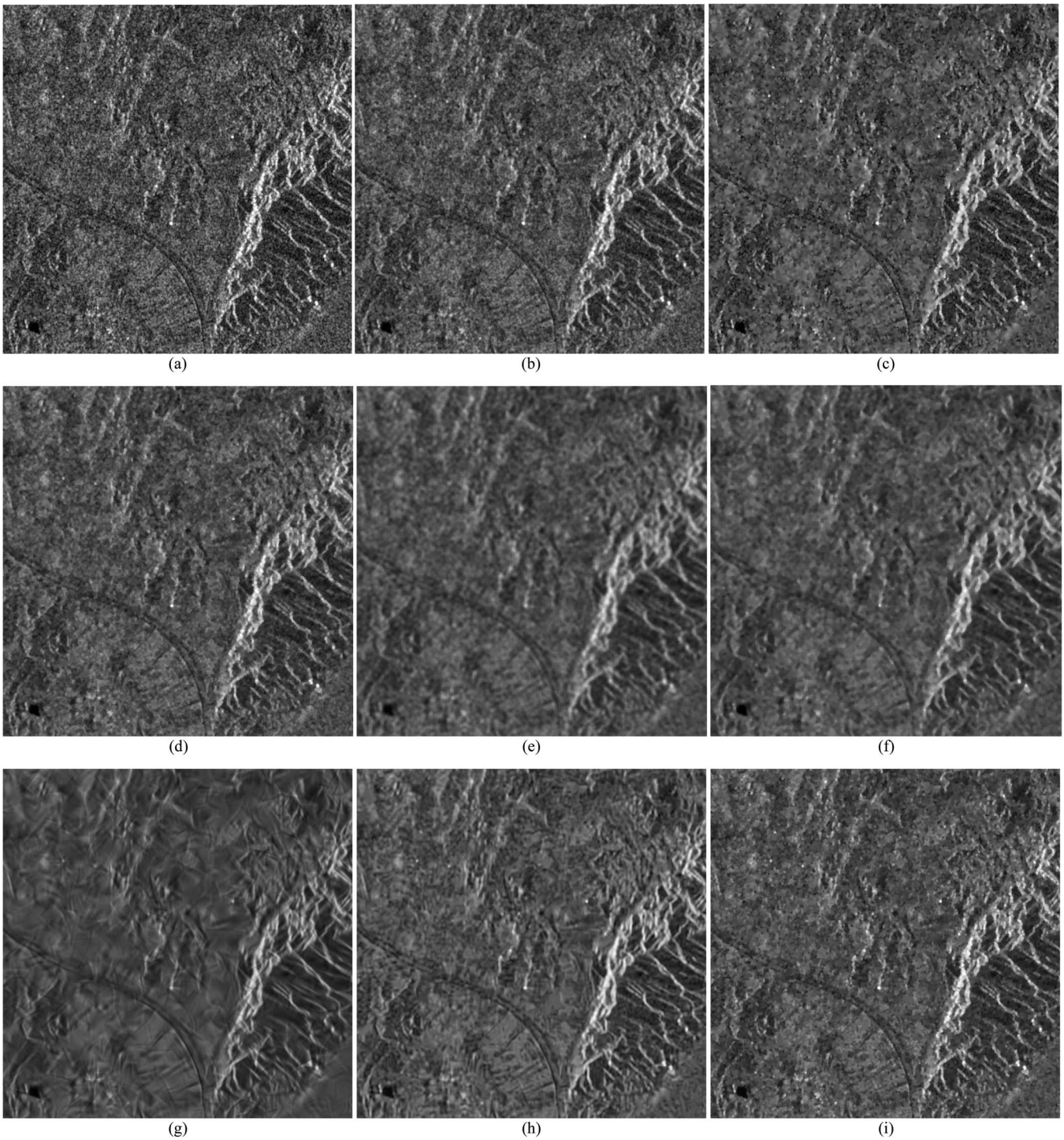


Fig. 5. Despeckling experimental results of an ERS C-band SAR image. The filters used in (b)–(f) are $5 \times 5$. (a) Original image. (b) Lee filter. (c) Frost filter. (d) Adaptive median filter. (e) Mean filter. (f) Median filter. (g) Shearlet transform. (h) Nonlocal filtering. (i) ATV regularization.

observation and the DEI suggest that the ATV algorithm is more loyal to the true ground feature information encoded in the speckles in SAR images. Visual assessment indicates that the DEI decreases with the improvement of despeckling from the original to adaptive median filter, Lee filter, Frost filter, shearlet transform, and mean filter and then further decreases with the improvement of edge sharpness from the median filter to nonlocal filtering and ATV regularization (Fig. 3 and Table IV).

Fig. 5 illustrates the despeckling results of a single-look ERS C-band SAR image of a coastal area with mountain and sea using the same algorithms as that for the ALOS SAR example. The original ERS image [Fig. 5(a)] looks very noisy, and its visual quality is badly degraded by speckles. It is interesting to notice that the despeckling performance of different techniques may be scene and SAR band dependent according to the DEI values in Table IV, where the performance ranking order is changed. For this image, nonlocal filtering is ranked behind

TABLE V
DEI VALUES CALCULATED FROM AN ALOS SAR IMAGE DESPECKLED BY EIGHT DESPECKLING METHODS USING DIFFERENT WINDOW SIZES OF NUMERATOR($m$)AND DENOMINATOR($n$)

| $m$ \ $n$ | **11** | **13** | **15** | **17** | **19** | **21** | **23** | **25** |
|---|---|---|---|---|---|---|---|---|
| | Lee | Lee | Lee | Lee | Lee | Lee | Lee | Lee |
| | Frost | Frost | Frost | Frost | Frost | Frost | Frost | Frost |
| | Mean | Mean | Mean | Mean | Mean | Mean | Mean | Mean |
| | Median | Median | Median | Median | Median | Median | Median | Median |
| | A-median | A-median | A-median | A-median | A-median | A-median | A-median | A-median |
| | Shearlet | Shearlet | Shearlet | Shearlet | Shearlet | Shearlet | Shearlet | Shearlet |
| | Nonlocal | Nonlocal | Nonlocal | Nonlocal | Nonlocal | Nonlocal | Nonlocal | Nonlocal |
| | ATV | ATV | ATV | ATV | ATV | ATV | ATV | ATV |
| **3** | 0.1945 | 0.1691 | 0.1508 | 0.1368 | 0.1258 | 0.1168 | 0.1093 | 0.1030 |
| | 0.1639 | 0.1435 | 0.1286 | 0.1172 | 0.1081 | 0.1007 | 0.0945 | 0.0891 |
| | 0.1221 | 0.1029 | 0.0895 | 0.0796 | 0.0720 | 0.0660 | 0.0611 | 0.0570 |
| | *0.0723* | *0.0546* | *0.0423* | *0.0333* | *0.0266* | *0.0213* | *0.0171* | *0.0138* |
| | 0.1608 | 0.1370 | 0.1196 | 0.1062 | 0.0956 | 0.0870 | 0.0798 | 0.0737 |
| | 0.1397 | 0.1176 | 0.1019 | 0.0902 | 0.0811 | 0.0738 | 0.0679 | 0.0629 |
| | 0.0905 | 0.0732 | 0.0614 | 0.0529 | 0.0465 | 0.0415 | 0.0374 | 0.0341 |
| | **0.0324** | **0.0241** | **0.0189** | **0.0155** | **0.0131** | **0.0113** | **0.0099** | **0.0088** |
| **5** | 0.3595 | 0.3188 | 0.2889 | 0.2660 | 0.2477 | 0.2328 | 0.2203 | 0.2097 |
| | 0.3387 | 0.3016 | 0.2743 | 0.2531 | 0.2362 | 0.2223 | 0.2106 | 0.2006 |
| | 0.2615 | 0.2242 | 0.1980 | 0.1784 | 0.1632 | 0.1510 | 0.1410 | 0.1326 |
| | 0.2409 | 0.2041 | 0.1780 | 0.1586 | 0.1435 | 0.1314 | 0.1215 | 0.1132 |
| | 0.3654 | 0.3263 | 0.2970 | 0.2742 | 0.2557 | 0.2405 | 0.2276 | 0.2166 |
| | 0.2841 | 0.2434 | 0.2139 | 0.1915 | 0.1739 | 0.1597 | 0.1479 | 0.1380 |
| | *0.2062* | *0.1692* | *0.1436* | *0.1249* | *0.1107* | *0.0995* | *0.0903* | *0.0827* |
| | **0.1582** | **0.1255** | **0.1032** | **0.0873** | **0.0753** | **0.0660** | **0.0586** | **0.0526** |
| **7** | 0.4654 | 0.4169 | 0.3800 | 0.3509 | 0.3275 | 0.3082 | 0.2921 | 0.2784 |
| | 0.4813 | 0.4323 | 0.3958 | 0.3673 | 0.3443 | 0.3253 | 0.3092 | 0.2954 |
| | 0.3906 | 0.3364 | 0.2979 | 0.2691 | 0.2465 | 0.2284 | 0.2135 | 0.2009 |
| | 0.3890 | 0.3353 | 0.2969 | 0.2679 | 0.2452 | 0.2270 | 0.2119 | 0.1992 |
| | 0.5022 | 0.4532 | 0.4163 | 0.3872 | 0.3637 | 0.3441 | 0.3275 | 0.3133 |
| | 0.4120 | 0.3562 | 0.3154 | 0.2842 | 0.2594 | 0.2393 | 0.2226 | 0.2084 |
| | *0.3274* | *0.2713* | *0.2320* | *0.2028* | *0.1804* | *0.1625* | *0.1479* | *0.1358* |
| | **0.3101** | **0.2555** | **0.2170** | **0.1884** | **0.1665** | **0.1490** | **0.1348** | **0.1231** |
| **9** | 0.5314 | 0.4834 | 0.4453 | 0.4141 | 0.3882 | 0.3663 | 0.3476 | 0.3314 |
| | 0.5938 | 0.5360 | 0.4925 | 0.4585 | 0.4309 | 0.4080 | 0.3885 | 0.3717 |
| | 0.5108 | 0.4414 | 0.3917 | 0.3542 | 0.3248 | 0.3012 | 0.2816 | 0.2652 |
| | 0.5167 | 0.4485 | 0.3995 | 0.3623 | 0.3331 | 0.3095 | 0.2899 | 0.2734 |
| | 0.6081 | 0.5512 | 0.5081 | 0.4741 | 0.4464 | 0.4232 | 0.4036 | 0.3866 |
| | 0.5244 | 0.4561 | 0.4058 | 0.3671 | 0.3363 | 0.3111 | 0.2902 | 0.2725 |
| | **0.4484** | **0.3747** | **0.3225** | **0.2833** | **0.2529** | **0.2161** | **0.2085** | **0.1917** |
| | *0.4520* | *0.3803* | *0.3291* | *0.2904* | *0.2603* | *0.2185* | *0.2360* | *0.1994* |

mean filter and median filter with slightly higher DEI, while the ATV is a clear-cut leading algorithm with the lowest DEI. Our visual assessment more favors to the nonlocal filtering result to be the second best as the mean filter result is noticeably blurred and the median filter result is less sharp than the nonlocal filtering. The fact of its higher DEI may be due to the visually stealth artifacts as revealed in Fig. 4(b) and patchwise over smoothness. In both SAR image processing examples, the shearlet transform was picked out by relatively high DEI values for its problem of introducing severe "ghost" textures, although the images may look impressive at first glance in nonfull resolution display.

To further investigate the robustness and validity of DEI to the variation of calculation window size, the DEI values are calculated from the despeckled ALOS SAR images (Fig. 3) of all of the algorithms tested using different window sizes as presented in Table V. The data in Table V show the same trend as shown in Table II: DEI increases with the increase of numerator window size and decreases with the increase of denominator window size; however, the DEI values of all of the algorithms in Table V are lower than that of the original image in Table II for the corresponding window size. As expected, the phenomena verify the principle of DEI defined in (5). For this image of a mountain-to-hill transition area, the despeckled image is locally smoother than the original image, but with the increase of numerator window size, edges are included to increase the standard deviation in the numerator of DEI and thus the value of DEI. The increase of denominator window size ensures more edges to be included and results in larger standard deviation in the denominator; thus, the DEI value decreases. In Table V, the lowest DEI values are in bold font, and the second lowest values are in italic font. We can observe that the ranking order of the DEI values for different algorithms changes with the increase of numerator window size but is stable with the increase of denominator window size. For all numerator window sizes, ATV has the lowest DEIs, except for $9 \times 9$, where the nonlocal filtering produced the lowest DEIs. For $3 \times 3$ numerator window, median filter has the second lowest DEIs for all of the denominator windows, while the nonlocal filtering ranks the third. The order drop of nonlocal filtering in $3 \times 3$ numerator window is again possibly caused by its edge enhancement artifacts that increase the standard deviation of the denominator in small window. While for $9 \times 9$ numerator window, the patchwise smoothness of nonlocal filtering is advantageous,

ensuring the lowest DEIs for all of the denominator windows. The ranking order for all of the algorithms maintains the same for numerator windows $5 \times 5$ and $7 \times 7$. This means that the DEI is most stable and robust within this numerator window range. Also, according to the experiments, using simulated speckled images, the minimum DEI of $5 \times 5$ numerator windows is at the position very close to the true noise $\sigma$ [Fig. 1(c)]. Although DEI is insensitive to the variation of denominator window size, the differentiation of despeckling performance becomes less significant when the denominator window is not significantly larger than the numerator window. We therefore recommend DEI calculation window size $5 \times 5$ for numerator and $19 \times 19$ for denominator.

## V. Conclusion

In this paper, we have presented an edge-preserving despeckling method based on the TV regularization model, with its regularization parameter adaptive to the noise level estimated by wavelets. We call the algorithm ATV. The noise removal using TV regulation is based on an additive noise model, while radar speckles are multiplicative. A logarithmic transformation of the SAR image is applied as the initial step of the ATV to convert the multiplicative speckles to an additive component that is statistically independent of the scene.

The ATV regularization despeckling method uses wavelets to estimate the noise level of a SAR image. The regularization parameter updates in every step of the iteration in relation to noise variance $\sigma$. The estimation of $\sigma$ can hardly be precise and unique; it varies with the types of wavelets used and the scene complexity. However, because of the adaptive optimization mechanism of the algorithm, an automatic rough estimation of $\sigma$ is adequate to initiate the despeckling within the near range of a global optimal and then to achieve the local optimization for edge preserve despeckling. Experiments indicate that the estimation of noise variance $\sigma$ in our method is robust and almost optimal.

To assess the performance of edge preserve despeckling for SAR images, the DEI is designed, which is based on the ratio of local standard deviations calculated from a small window for the numerator and large window for the denominator. In principle, the DEI indicates a better edge-preserving despeckling performance by a lower value. The window sizes for the numerator and denominator of DEI can be determined empirically for optimal sensitivity, but DEI is fairly robust to considerable variation of the window size. The experiments using simulated speckled images and ALOS L-band SAR and ERS C-band SAR images demonstrated that the quantitative indication by DEI values matches the visual assessment for five conventional despeckling filters in comparison. Always with the lowest DEIs, the ATV results show obvious better visual quality in terms of despeckling smoothness and edge sharpness. It is interesting to notice that the DEI consistently indicates the simple median filter as a competent performer for despeckling.

For further test, we have compared the ATV with two recent new despeckling algorithms: shearlet transform and wavelet-based nonlocal filtering. Shearlet transform is effective for despeckling; however, it introduces severe artifacts of "ghost" textures which do not exist in the original images. This defect has been effectively indicated by rather high DEI values. The despeckling results from nonlocal filtering are visually more appealing than those from ATV in terms of patchwise smoothness and edge sharpness, but ATV always achieves the lowest DEI. The investigation then revealed that the nonlocal filtering algorithm introduces subtle artifacts of horizontal ripples and homogenous blobs. The finding implies that ATV is more loyal to original images, not compromising fidelity for good looking. It also demonstrates that DEI is diagnostic to the true quality of edge preserve despeckling for SAR images. The ATV is simple in concept, fast in computing, and straightforward in operation without user-tuned parameters. Achieving consistent good performance for SAR image despeckling at high speed, ATV is practical for real applications.

## References


[1] C. Oliver and S. Quegan, *Understanding Synthetic Aperture Radar Images*. Norwood, MA, USA: Artech House, 1998.

[2] J. S. Lee, "Refined filtering of image noise using local statistics," *Comput. Graph. Image Process.*, vol. 15, no. 4, pp. 255–269, Apr. 1981.

[3] V. S. Frost, J. A. Stiles, K. S. Shanmugan, and J. C. Holtzman, "A model for radar images and its application to adaptive digital filtering of multiplicative noise," *IEEE Trans. Pattern Anal. Mach. Intell.*, vol. PAMI-4, no. 2, pp. 157–166, Mar. 1982.

[4] D. Kuan, A. Sawchuk, T. Strand, and P. Chavel, "Adaptive noise smoothing filter for images with signal-dependent noise," *IEEE Trans. Pattern Anal. Mach. Intell.*, vol. PAMI-7, no. 2, pp. 165–177, Mar. 1985.

[5] M. Dai, C. Peng, A. Chan, and D. Loguinov, "Bayesian wavelet shrinkage with edge detection for SAR image despeckling," *IEEE Trans. Geosci. Remote Sens.*, vol. 42, no. 8, pp. 1642–1648, Aug. 2004.

[6] F. Argenti and L. Alparone, "Speckle removal from SAR images in the undecimated wavelet domain," *IEEE Trans. Geosci. Remote Sens.*, vol. 40, no. 11, pp. 2363–2374, Nov. 2002.

[7] H. Xie, L. Pierce, and F. Ulaby, "Despeckling SAR images using a low-complexity wavelet denoising process," in *Proc. IGARSS*, 2002, pp. 321–324.

[8] D. Gleich, M. Kseneman, and M. Datcu, "Despeckling of TerraSAR-X data using second-generation wavelets," *IEEE Geosci. Remote Sens. Lett.*, vol. 7, no. 1, pp. 68–72, Jan. 2010.

[9] B. B. Saevarsson, J. R. Sveinsson, and J. A. Benediktsson, "Speckle reduction of SAR images using adaptive curvelet domain," in *Proc. IGARSS*, 2003, pp. 4083–4085.

[10] B. Hou, X. Zhang, X. Bu, and H. Feng, "SAR image despeckling based on nonsubsampled shearlet transform," *IEEE J. Sel. Top. Appl. Earth Obs.*, vol. 5, no. 3, pp. 809–823, Jun. 2012.

[11] W. Zhang *et al.*, "SAR image despeckling using edge detection and feature clustering in bandelet domain," *IEEE Geosci. Remote Sens. Lett.*, vol. 7, no. 1, pp. 131–135, Jan. 2010.

[12] F. Argenti, T. Bianchi, and L. Alparone, "Multiresolution MAP despeckling of SAR images based on locally adaptive generalized Gaussian pdf modeling," *IEEE Trans. Image Process.*, vol. 15, no. 11, pp. 3385–3399, Nov. 2006.

[13] S. Parrilli, M. Poderico, C. V. Angelino, G. Scarpa, and L. Verdoliva, "A nonlocal SAR image denoising algorithm based on LLMMSSE wavelet shrinkage," *IEEE Trans. Geosci. Remote Sens.*, vol. 50, no. 2, pp. 606–616, Feb. 2012.

[14] L. Rudin, S. Osher, and E. Fatemi, "Nonlinear total variation based noise removal algorithms," *Phys. D, Nonlinear Phenomena*, vol. 60, no. 1–4, pp. 259–268, Nov. 1992.

[15] D. L. Donoho, "Compressed sensing," *IEEE Trans. Inf. Theory*, vol. 52, no. 4, pp. 1289–1306, Apr. 2006.

[16] J. Cai, B. Dong, S. Osher, and Z. Shen, "Image restoration: Total variation, wavelet frames, and beyond," *J. Amer. Math. Soc.*, vol. 25, no. 4, pp. 1033–1089, 2012.

[17] D. Donoho and J. Johnstone, "Ideal spatial adaptation by wavelet shrinkage," *Biometrika*, vol. 81, no. 3, pp. 425–455, 1994.

[18] S. Becker, J. Bobin, and E. J. Candes, "NESTA: A fast and accurate first-order method for sparse recovery," *SIAM J. Imaging Sci.*, vol. 4, no. 1, pp. 1–39, 2011.

[19] C. Vogel and M. Oman, "Iterative method for total variation denoising," *SIAM J. Sci. Comput.*, vol. 17, no. 1, pp. 227–238, 1996.
[20] W. Yin, S. Osher, D. Goldfarb, and J. Darbon, "Bregman iterative algorithms for l1-minimization with applications to compressed sensing," *SIAM J. Imag. Sci.*, vol. 1, no. 1, pp. 143–168, 2008.
[21] A. Chambolle, "An algorithm for total variation minimization and applications," *J. Math. Imag. Vision*, vol. 20, no. 1/2, pp. 89–97, Jan. 2004.
[22] G. Peyre, Total Variation Regularization with Chambolle Algorihtm. [Online]. Available: http://www.coe.utah.edu/~cs7640/readings/TotalVariationRegularizationwithChambolleAlgorihtm.pdf

**Yao Zhao** received the Bachelor's degree in information and computing science and the Ph.D. degree in applied mathematics from BeiHang University of Aeronautics and Astronautics, Beijing, China, in 2006 and 2011, respectively.

He is currently a Postdoctor with the University of Chinese Academy of Sciences, working in the Science and Technology on Microwave Imaging Laboratory, Institute of Electronics, Chinese Academy of Sciences, Beijing. His main research interests include radar signal processing, compressed sensing, and wavelets.

**Jian Guo Liu** (M'10) received the M.Sc. degree in remote sensing and geology from China University of Geosciences, Beijing, China, in 1982 and the Ph.D. degree in remote sensing and image processing from Imperial College London, London, U.K., in 1991.

He is a Reader in remote sensing with the Department of Earth Science and Engineering, Imperial College London. His current research activities are subpixel technology for image registration, DEM generation and change detection, image processing techniques for data fusion, filtering and InSAR, and GIS multidata modeling for geohazard studies.

**Bingchen Zhang** received the Bachelor's degree from the University of Science and Technology of China, Hefei, China, in 1996 and the M.S. degree from the Institute of Electronics, Chinese Academy of Sciences (IECAS), Beijing, China, in 1999.

Since 1999, he has been a Scientist with IECAS. His main research interests are synthetic aperture radar (SAR) signal processing and airborne SAR system design, implementation, and data processing.

**Wen Hong** (M'03) received the M.S. degree in electronic engineering from Northwestern Polytechnical University, Xian, China, in 1993 and the Ph.D. degree from BeiHang University, Beijing, China, in 1997.

Since 2002, she has been a Scientist with the Science and Technology on Microwave Imaging Laboratory, Supervisor of the graduate student program, and Administrative Vice Director of the Institute of Electronics, Chinese Academy of Sciences, Beijing. Her main research interests are polarimetric/polarimetric interferometric synthetic aperture radar data processing and application, 3-D synthetic aperture radar (SAR) signal processing, circular SAR signal processing, and sparse microwave imaging with compressed sensing.

**Yi-Rong Wu** (M'00) received the Ms.D. degree from the Beijing Institute of Technology, Beijing, China, in 1988 and the Ph.D. degree from the Institute of Electronics, Chinese Academy of Sciences (IECAS), Beijing, China, in 2001.

Since 1988, he has been with IECAS, where he currently serves as the Director. He has over 20 years of experience in remote-sensing processing system design. His current research interests are microwave imaging, signal and information processing, and related applications.